34

Remote Sensing Rock Mechanics and Earthquake Thermal Infrared Anomalies

Lixin Wu[1,2] and Shanjun Liu[2]
[1]*Academy of Disaster Reduction & Emergency Management, Beijing Normal University, Beijing, China*
[2]*Institute for Geo-informatics & Digital Mine Research, Northeastern University, Shenyang, China*

1. Introduction

Rock fracturing is the cause of many geo-hazards including tectonic earthquake (EQ), rock burst, rock sloping and rock pillar failure. Radiation signals such as acoustic emission, radio frequency emission and electromagnetic (EM) radiation from loaded deforming rock, are able to provide useful information for monitoring, interpreting and predicting rock fracturing (Renata, 1977; Brady and Rowell, 1986; Yamada et al., 1989; Martelli et al., 1989). Based on thermo-elastic theory, thermo-elastic stress analysis (TSA) and stress pattern analysis by thermal emission (SPATE) were developed for the stress measurement of solid materials, including homogeneous metal, macromolecular and composite materials, respectively in 1960's and 1970's (Mounatin and Webber, 1978). Luong applied thermovision to study experimentally the damage processes of concrete and rock (Luong, 1990), but no reach to the remote sensing on geo-hazards.

In the experiments for investigating the mechanism of satellite thermal infrared (TIR) anomaly before tectonic EQ (Gorny et al., 1988; Qiang et al., 1990), it was discovered that there do exist TIR anomaly before rock fracturing (Geng et al., 1992). Later, it was furthermore discovered that there are obvious TIR features as precursors of rock fracturing, and that the loaded stress around $0.79\sigma_c$ can be taken as a precaution index for the stability monitoring of loaded rocks (Wu and Wang, 1998). To explore the laws of infrared radiation (IRR) variation in the process of rock loading, deforming and fracturing, and to reveal the possible mechanism of satellite TIR anomaly before EQ, a large amount of IRR imaging experiments on rock loaded to fracturing were conducted in China (Wu et al., 2000, 2001, 2002, 2003, 2004a, 2004b, 2004c, 2004d, 2006a, 2006b; Deng et al., 2001; Liu et al., 2002). Hence, a new intersection discipline, Remote Sensing Rock Mechanics (RSRM), which takes Remote Sensing, Rock Mechanics, Rock Physics and Informatics as its foundations and serves for remote sensing on geo-hazards, was originated (Geng et al., 1992; Wu et al., 2000).

Based on retrospection to past experiments on RSRM, it was pointed out that there are two IRR anomalies, being IRR image anomaly and IRR temperature curve anomaly respectively, can act as rock fracturing precursors. The average IRR temperature (AIR*T*), being the

integral reflection of surface IRR energy, is applied as a quantitative index to study the temporal evolution of IRR from loaded rock and to seek for the potential precursors of rock fracturing. The temporal evolution of AIR*T* are the comprehensive effect of a series of physical-mechanical processes inside a loaded rock, such as rock thermo-elastic acting, pore gas desorbing & escaping, fractures producing & extending, rock frictionating, heat transferring and environment radiation. The thermo-elastic effect and the frictional thermal are two of the main mechanisms of increased IRR from loaded rock. RSRM experiments had revealed the laws of changed IRR from loaded rock and provided scientific interpretations for the mechanisms of satellite TIR anomaly before tectonic EQs of Ms>5.5.

2. Remote Sensing Rock Mechanics Experiments

2.1 Experiment Methods and Tools

The typical RSRM experiment is comprised of a loader (uni-axial or bi-axial), an infrared imager and rock samples. As in Figure 1, a bi-axial loader was applied for loading along two directions, and an infrared imager was applied to detect the surface IRR from loaded rock. The maximum imaging rate of the imager is 60f/s, and the recording rate was usually set as 1f/s to record the IRR images continuously. Usually, tectonic EQ might be resulted from the suddenly fracturing of compressively-sheared crust rock, the suddenly breaking of faults at disjointed zones, the suddenly sliding of compressively-sheared faults or the stability losing of compressively loaded intersected faults. To simulate the different mechanisms of rock fracturing and EQ, several typical loading schemes were applied as in Figure 1.

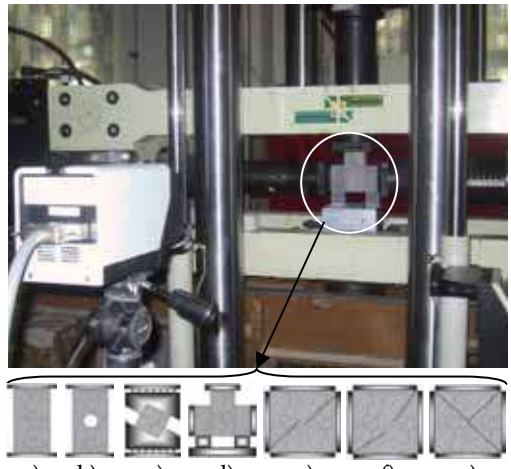

Fig. 1. RSRM experiment schemes to simulate different mechanisms of rock fracturing or tectonic EQ: a) uni-axially load on a standard cylinder rock sample; b) uni-axially load on a cylinder rock sample with a central hole; c) compressively-sheared load on a hexahedral rock sample; d) bi-axially load on three jointed rock samples to frictional sliding; e) bi-axially load on a damage rock sample with en echelon faults; f) bi-axially load on a damage rock sample with disjointed faults; and g) bi-axially load on three jointed rock samples simulating intersected faults.

2.2 Rock Fracturing Precursor: IRR Image Anomaly

2.2.1 Uni-axially loaded rock

Lots of rock samples made from coal, ironstone, sandstone, marble, limestone, granite, granodiorite, gabbro and gneiss were uni-axially loaded and thermal imaging detected. The sample size was standard of diameter and length, respectively, 50 and 100mm. It was discovered that the IRR images of the uni-axially loaded rock have different features for different fracturing pattern (Wu et al., 2006a). As in Figures 2~4, there are three fracturing patterns, "X"-shaped, "//"-shaped and "|"-shaped respectively, occurred in our experiments. The "X"-shaped and "//"-shaped positive IRR abnormal strips foretell the coming of "X"-shaped shearing fracturing and the coming of "//"-shaped shearing fracturing respectively, while the "|"-shaped negative IRR abnormal strip foretells the coming of tensile fracturing.

The "X"-shaped positive IRR abnormal strips generated with loading along the "X"-shaped shearing zone before peak stress, and got distinguished after peak stress, as in Figure 2. The rock sample got finally fractured along the "X"-shape shearing zone. The evolution of IRR abnormal strip had also reflected the fracturing being not symmetrical upper-and lower, in that the upper part was clear with higher temperature, while the lower part is fuzzy with lower temperature.

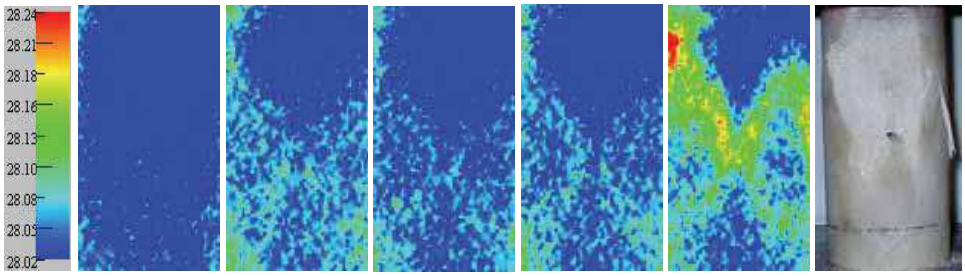

Fig. 2. The IRR image positive anomaly of "X"-shaped shearing fracturing of an uni-axially loaded marble sample

The "//"-shaped positive IRR abnormal strips generated with loading along the "//'-shaped shearing zone at the upper part of sample before peak stress, and got distinguished after peak stress, as in Fig 3. The evolution of the positive IRR image anomaly had also reflected the fracturing being not symmetrical in that the upper part of the IRR anomaly strip was clear with higher temperature, while the lower part was fuzzy excepting for the final fracturing near the bottom of the sample. Besides, there was strong IRR anomaly spot at the fracturing center for the intensive accumulation of mechanical energy and for the intensive generation of frictional thermal at the local central place.

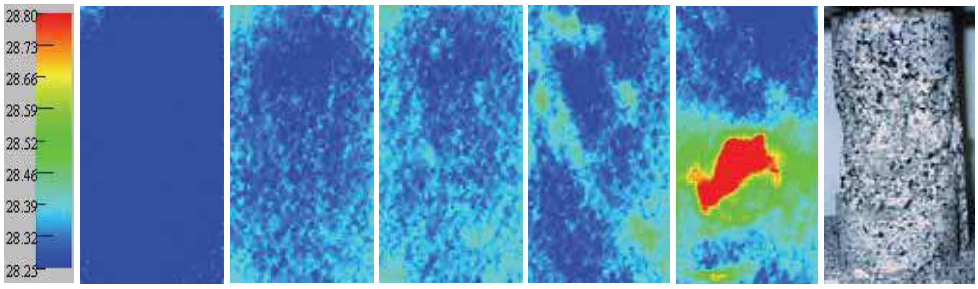

Fig. 3. The IRR image positive anomaly of "//"-shaped shearing-fracturing of an uni-axially loaded granite sample

The "|"-shaped negative IRR abnormal strip generated with loading along the tensile fracturing zone of a rock sample before the peak stress, and got distinguished gradually at the peak stress and after fracturing, as the approximately vertical dark strip in Figure 4. The same phenomenon for a sandstone sample with a calcite vein was also reported (Wu, et al., 2000).

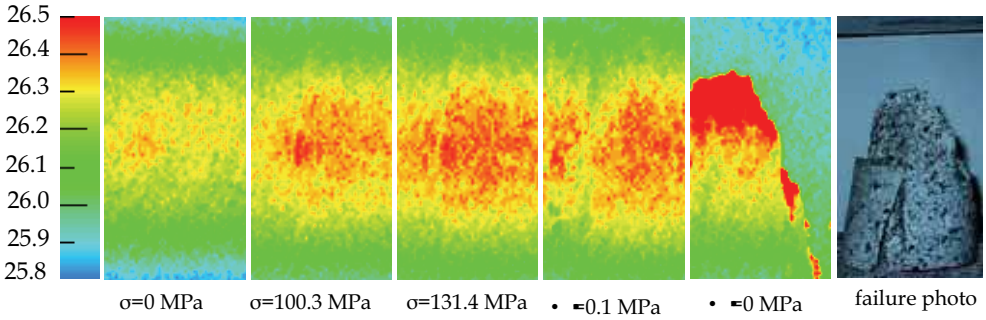

Fig. 4. The IRR image negative anomaly of "|"-shaped tensile fracturing of an uni-axially loaded granite sample

2.2.2 Uni-axially loaded rock with a central hole

More than 10 samples with a central hole, modeling the structure stability of loaded rock tunnels, made from marble and granite were infrared imaging detected. The rock samples had two kinds of shapes respectively being cylinder with diameter and length, respectively, 50 and 100mm, and regular block with thickness, width and length, respectively, 70, 35 and 100 mm. It was discovered that there were distinguished positive IRR image anomalies before rock fracturing, and the place of anomaly were exactly the coming fracturing place. As in Figure 5, the positive IRR image anomalies had reflected the two kinds of fracturing, respectively being diagonal fracturing (sample 1~5) and fork fracturing (sample 6). The IRR anomalies, along the fracturing planes and shaped as spots or strips, generated not only on rock surface but also on the hole's surface (lateral sample 4 and 5). The temperature increment is 1~3°C and 4~8°C respectively for marble and granite samples.

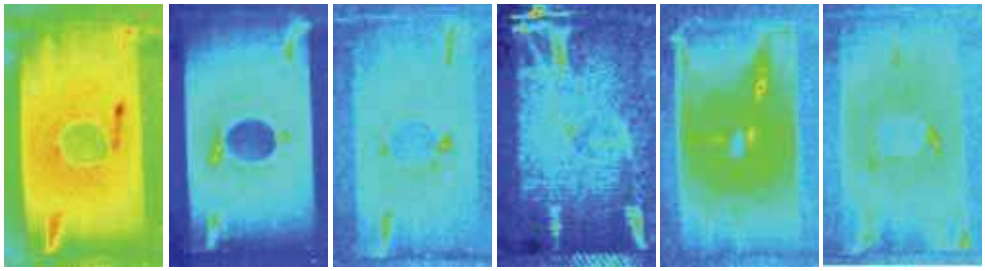

Fig. 5. The IRR image positive anomalies of a group of uni-axially loaded marble samples with a central hole

2.2.3 Compressively sheared rock

More than 20 samples, size 7×7×7×cm^3, made from sandstone, marble, limestone, granite and gneiss, were compressively sheared and infrared imaging detected. Three pairs of steel platens with shearing angle being 45°, 60° and 70° respectively were applied. The loading rate was controlled as 2~5kN/s. It was discovered that the IRR temperature of rock surface changed with loading, and a strip-shaped positive IRR image anomaly generated along the central shearing plane before fracturing. With loading, the positive abnormal strip got more and more distinguished and migrated gradually from the upper end to the lower end of the sample, which foretold that the compressive-shearing fracturing was developing gradually from the upper end to the lower end of the sample along the central shear plane. Figure 6 shows the typical IRR image series of a compressively sheared limestone sample.

As a special geological phenomenon occurring with the formation of great fault, penniform-shaped fractures are a group of secondary fractures produced with the formation of great primary fracture (Nicolas et al., 1977). It happened to occur in our experiments that there were penniform-shaped fractures produced with a primary fracture in the compressive loaded rock samples, as in Figure 7. The IRR positive anomaly strips generated aside the primary IRR strip, passing through the central shearing plane, had reflected the penniform-shaped fracturing events.

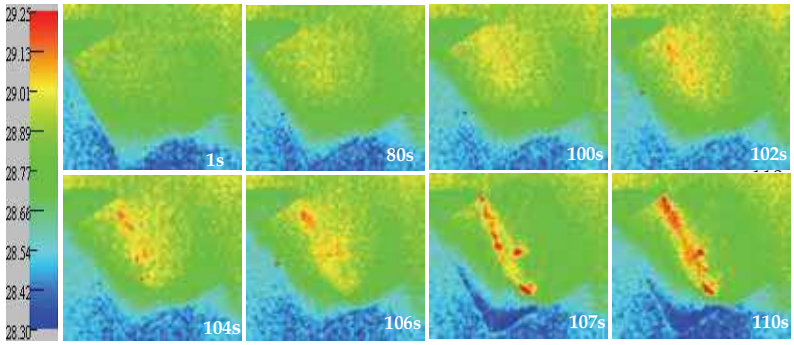

Fig. 6. The IRR image positive anomaly of the fracturing of a compressively sheared limestone sample (time in second)

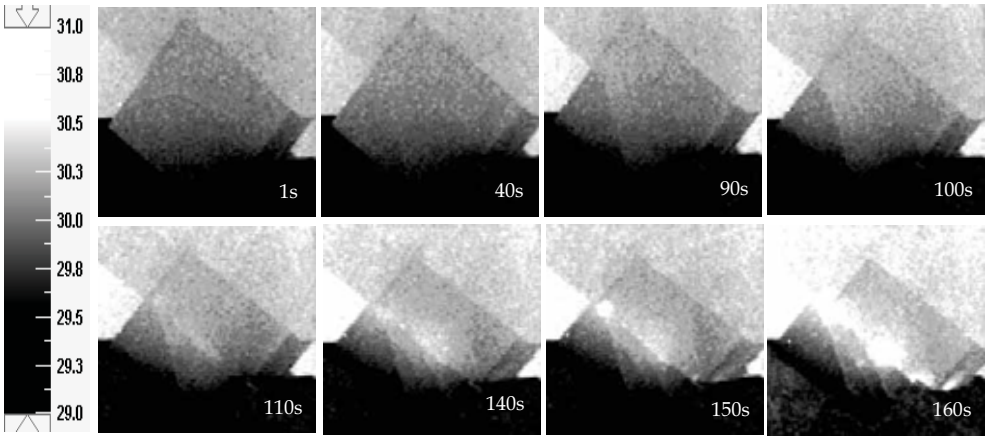

Fig. 7. The IRR image anomaly of the penniform-shaped fracturing of a compressively sheared marble sample

2.2.4 Bi-sheared frictional sliding rock blocks

Ten groups of rock samples made from gabbro, granodiorite, limestone and marble were IRR detected in the process of bi-sheared frictional sliding or viscosity sliding. Each group, as in Figure 8 and 9, was comprised of three jointed rock blocks whose size respectively be 50• 50• 100mm^3, 50• 70• 150mm^3 and 50• 50• 100mm^3 from left to right, and its friction area was constant, 50• 100mm^2. Four contact conditions, symmetrical (yes for rock property and for its smooth friction surface, as in Figure 8), uncertain symmetrical (yes for rock property but not for its coarse friction surface, as in Figure 9), unstable asymmetrical (yes for rock property but not for its staged friction surface) and stable asymmetrical (not for rock property but yes for its smooth friction surface), were designed and tested respectively (Wu et al., 2004b).

It is revealed that the evolution of rock surface IRR temperature field is not only correlated with rock stress, but also correlated with the features of friction surface and rock properties at both sides. General law lies in that the IRR at the place of stress concentration and strong friction zone is stronger than that at the place of stress relaxation and weak friction zone. In condition of friction surface be symmetrical, the IRR image is double butterfly-wings shaped, as in Figure 8. However, in condition of friction surface be uncertain symmetrical, unstable asymmetrical or stable asymmetrical, the temporal-spatial evolution of IRR anomaly is uncertain or unstable, as in Figure 9. The positive IRR anomaly spots, foretelling the evolution of stress, energy and viscosity-sliding process, may be beads-shaped, needle-shaped, suspended needle-shaped, strip-shaped, single butterfly-wings shaped or its evolution in order (Wu et al., 2004b).

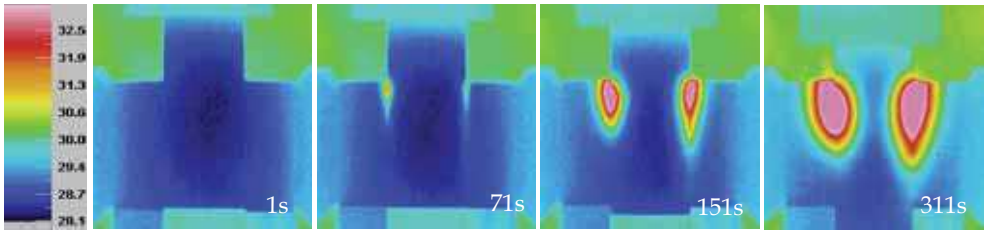

Fig. 8. The IRR image positive anomaly of the stick-slipping of symmetrical rock samples (time in second)

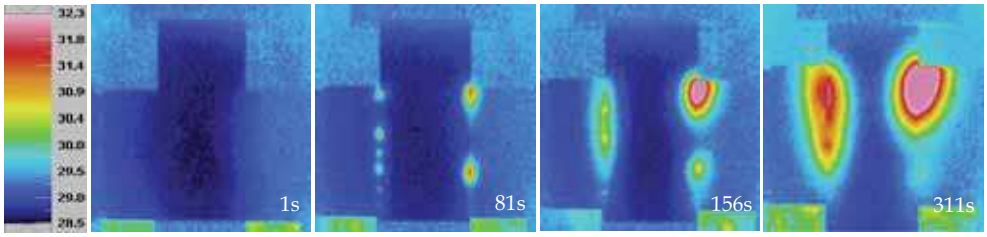

Fig. 9. The IRR image positive anomaly of the stick-slipping of asymmetrical rock samples (time in second)

2.2.5 Bi-axially loaded rock

Infrared imaging detection on the rupturing of en echelon and collinearly disjointed jointed faults were done in the process of bi-axial loading. It was revealed that the IRR from loaded rock surface is correlated with loading stress, which could be divided into five stages as loading beginning, linear elastic, stress locking, stress unlocking and fracturing(Wu et al., 2004a). During the stress-unlocking stage, positive IRR anomaly strip generated at the disjointed zone, as in Figure 10 and 11. The positive IRR anomaly strip around the disjointed zone has general evolution features as: firstly, the strip gets enhancing; then, gets weakening (or 'silence'); and finally, gets enhancing again. The re-enhancing of IRR anomaly strip after the weakening stage is a meaningful precursor foretelling the place of primary fracturing of faults or the coming epicenter of an EQ.

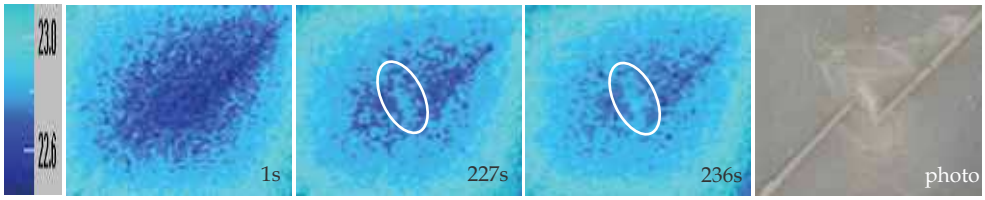

Fig. 10. The local IRR positive anomaly foretell the fracturing of en echelon disjointed faults (marble, time in second)

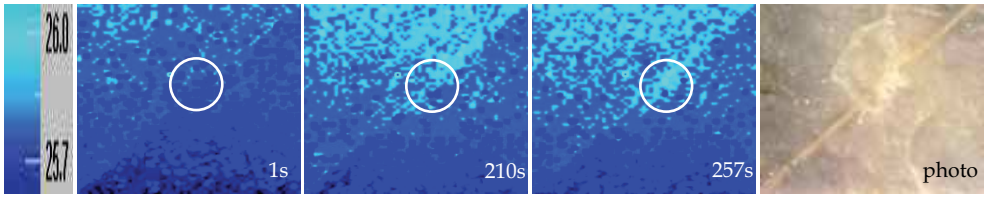

Fig. 11. The local IRR positive anomaly foretell the fracturing of collinearly disjointed faults (marble, time in second)

2.3 Rock Fracturing Precursor: IRR Temperature Anomaly

2.3.1 Quantitative index: AIR*T*

The evolution of surface IRR from loaded rock is the comprehensive effect of rock thermo-elastic acting, pore gas desorbing & escaping, fractures producing & extending, rock frictionating, heat transferring and environment radiation. Being the integral reflection of surface IRR energy, the average IRR temperature (AIR*T*) is selected as a quantitative index to study the evolution of IRR from loaded rock and to seek for rock fracturing precursors (Wu et al., 2006b).

The infrared imager detects and records the thermal images of loaded rock surface. The thermogram is comprised of a matrix of color pixels which representing the IRR brightness temperature of each pixel of the rock surface. For example, the imaging matrix of TVS-8100MKII infrared imager is 160• 120. The IRR temperature of each pixel tends to fluctuate with time due to the instability of the detector unit and the influence of environmental radiation, and the IRR temperature of each pixel will not always be the same for the local difference of rock stress and rock strain. The maximum, minimum and average value of loaded rock surface IRR temperature, respectively being IRRT_{max}, IRRT_{min} and IRRT_{ave}, could be quantitatively obtained from thermogram. The analysis revealed that IRRT_{max} and IRRT_{min} will not change obviously except that IRRT_{max} might rise suddenly just before rock fracturing, while IRRT_{ave} is to change stably with loading, as in Figure 12. The physical interpretation lies in that the surface IRRT_{ave} is a general reflection of the energy balance inside the loaded rock.

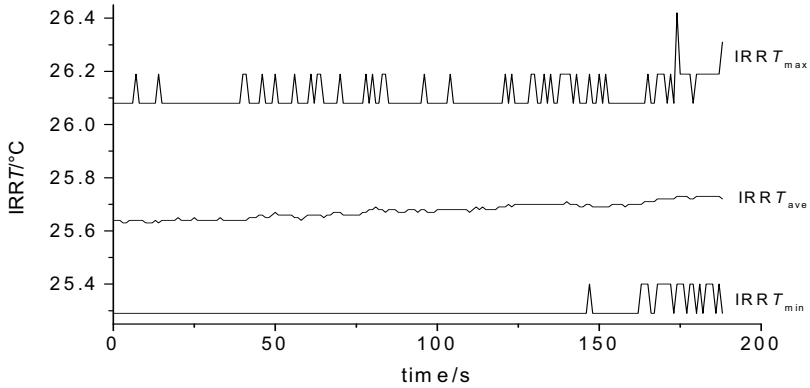

Fig. 12. The evolution of three indexes of IRR brightness temperature of loaded rock surface

Hence, the IRRT_{ave} of rock surface, denominated as AIR*T*, is selected as a quantitative index to study the precursors of rock fracturing and geo-hazards. The procedures for AIR*T*-based precursor analysis includes: 1) to define a unified boundary of the analyzed region (resampling region) for all thermograms; 2) to resample the IRR temperature value from the data file of each thermogram in time order; 3) to calculate the AIR*T* of the resampling region of each thermogram; 4) to draw the AIR*T*–time curve of the rock sample; 5) to analyze the evaluation features of the AIR*T*–time curve and to identify the messages as a precursor of rock fracturing and hazard; 6) to compare with the qualitative image anomaly so as to analyze and to confirm the AIR*T* abnormal precursor.

2.3.2 Influence factors of AIR*T* curves

1) Loading stages and rock deformation

The stress-strain curve is a basic method for describing rock deformation and for interpreting rock mechanical behaviors (Hudson and Harrison, 1997). Generally, the deformation process of loaded rock is divided into four stages respectively being stage-I of defects compaction, stage-II of linear elastic deformation, stage-III of plastic deformation and stage-IV of fracturing failure, as in Figure 13. The four characteristic points, E, Y, P and F are called as elastic-starting point, yield-starting point, peak-stress point and failure-impending point respectively.

Stage-I: the downward-concave curve section tells that there are some defects such as pores, fissures and joints inside the rock body, and that the defects is under compaction, which cause the stress to rise slowly. The more the defects, the severe the curve downward concave.

Stage-II: the curve section linearly developed tells that the compaction of defects has finished and the rock is undergoing elastic deformation. The higher the angle of the section line inclined, the stronger the rock.

Stage-III: the upward-concave curve section tells that there are new fractures developing inside the rock. The plastic deformation starts, and the new generated fractures together with the initial defects are possible to cause friction between its two side-faces.

Stage-IV: the curve section turning to drop tells that the fractures are getting wider, longer and to connect with each other. The rock is losing its strength and stability, and the final fracturing failure or rock hazard is impending.

For the difference between rock compositions, the details of stress-strain curve of different rock will be different. As to brittle rock, its stage-II is close to point P and its stage-IV will be cliff-shaped. Usually, most of the crust rocks are brittle. Five kinds of typical crust rock, granodiorite, gabbro, gneiss, limestone and marble had been tested in our experiments. The typical load-displacement curves of the tested rock samples are shown in Figure 14. It tells that all the tested rocks are brittle.

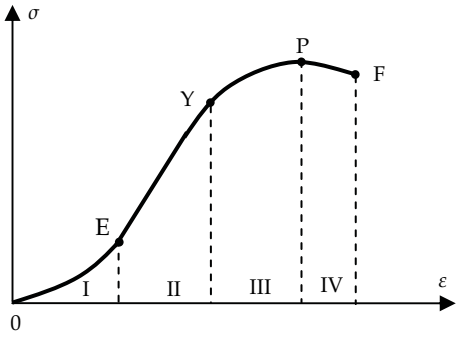

Fig. 13. Typical AIR*T* curve of uni-axially loaded rock

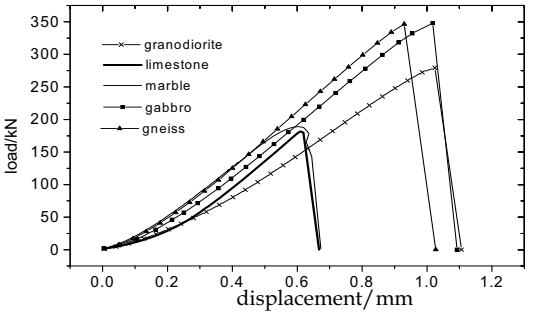

Fig. 14. The load-displacement curves of five tested rocks

2) The influence of loading condition

The experiments discovered that the evolutions of AIR*T* have different laws in different loading condition, such as uni-axial loading (constant displacement controlled), compressively-sheared loading (approximately constant load controlled) and bi-axial loading (constant displacement controlled).

a) Uni-axial loading

As shown in the left-hand side of Figure 15, the surface facing to the infrared imager is to be detected, and a rectangle region close to the boundary of the rock sample is defined for data resampling and analyzing (Liu et al., 2002; Wu et al., 2002). Multiple experiments revealed that there was slight variation of AIR*T* at different deformation stage although the AIR*T* linearly increased with load and deformation. At stage-I, the AIR*T* will rise slowly or drop a little; at stage-II, the AIR*T* will rise stably; at stage-III, the AIR*T* will rise quickly than that in stage-I and stage-II. The right-hand side of Figure 15 shows the comparison of the evolution of AIR*T* and the load with rock deformation, which is rock displacement in generally, of a marble sample.

b) Compressive-shear loading

In condition of compressively shear, the rock sample will always get fracturing along the shearing plane, which locates near to the central plane of the loaded sample. To minimize data resampling work and to focus on the key region, a narrow rectangle along the shearing plane is defined as the resampling and analyzing region (Wu et al., 2004c). Multiple experiments revealed that the temporal evolution of the AIR*T* is different with the shearing angle. Three shearing angles (γ) being 45°, 60° and 70° respectively, are applied. As the shearing angle changes from 45° to 70°, the temporal evolution changes from monotonic rise, to drop-to-rise and to monotonic drop in order, as in Figure 16.

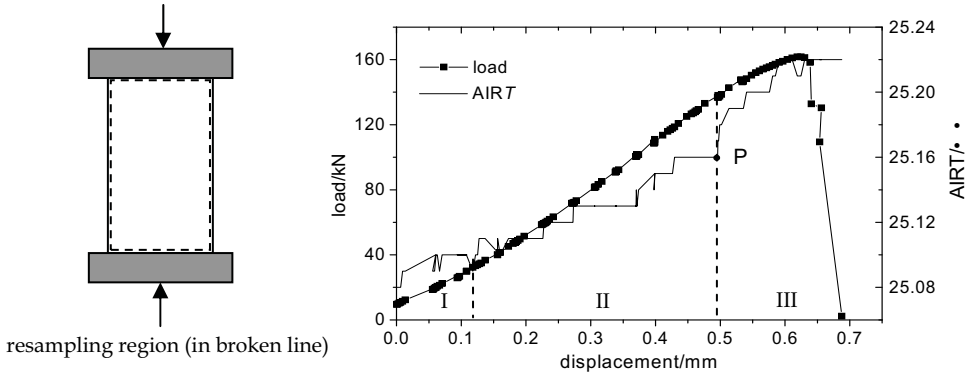

Fig. 15. The typical AIR*T* curve of uni-axially loaded rock sample (marble)

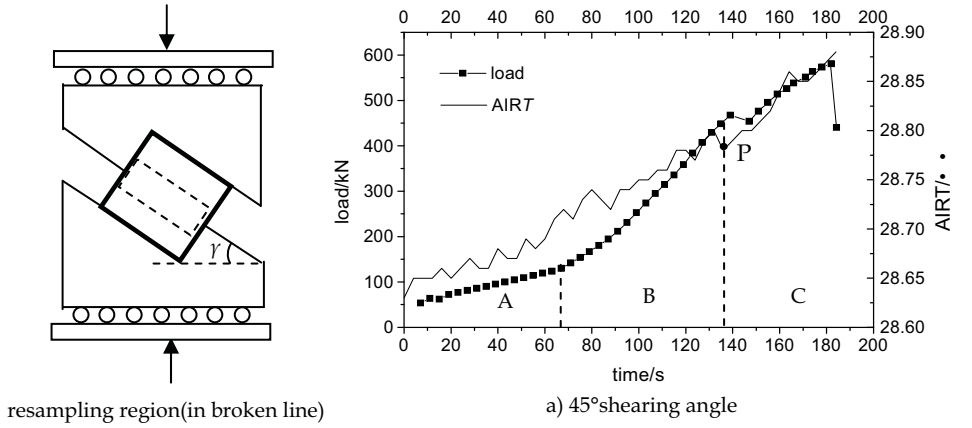

a) 45°shearing angle

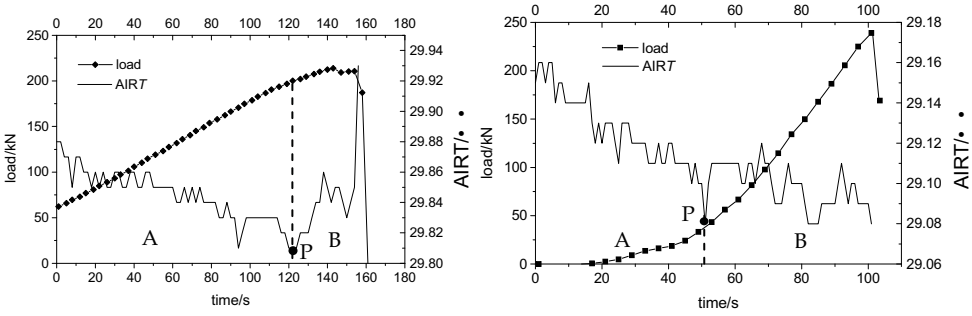

b) 60°shearing angle c) 70°shearing angle

Fig. 16. The typical AIR*T* curve of compressively-sheared rock samples at different shearing angles

The mechanism lays in that the ratio of compressive-stress to shear-stress along the shearing plane decrease with the rise of the shearing angle. The smaller is the shearing angle, the higher is the compression-shear ratio. In condition of 45°, the load-time curve developed in three stages, as stage A, B and C in Figure 16a, with load increasing from slow to rapid, and to slow again. In condition of 60° the load-time curve developed in two stages, as stage A and B in Figure 16b, with load speed changing from approximate constant to be decrease slightly. In condition of 70°, the load-time curve developed in two stages, as stage A and B in Figure 16c, with loading speed changing from slow to rapid.

The compressive action on loaded rock is to cause surface IRR temperature rise, while the tensile action on loaded rock is to cause surface IRR temperature drop. Actually, both compressive action and tensile action are to occur along the compressively sheared plane, and the detected surface IRR is the comprehensive effect of the two actions. It was reached that (Wu et al., 2004c): 1) in condition of shearing angle being 45°, the surface AIR*T* will rise monotonically with loading in that the temperature increment from compressive action and friction is stronger than the temperature decrement from tensile action in the whole loading process; 2) in condition of shearing angle being 60°, the surface AIR*T* will drop monotonically with loading in that the temperature increment from compressive action and friction is weaker than the temperature decrement from tensile action before stage-III (point Y in Figure 13, and point P in Figure 16b); with the friction effect getting strong in stage-III, the surface AIR*T* will get to rise in that the temperature from compression and friction get stronger than the temperature decrement from tensile action; 3) in condition of 70°, the surface AIR*T* will drop monotonically with loading in that the temperature increment from both compression and friction are weaker than the temperature decrement from tensile action.

c) Biaxial loading

By using of bi-axial loading system and infrared imaging system, the IRR features of two kinds of disjointed jointed faults, respectively be collinearly and non-collinearly disjointed faults, were experimentally studied (Wu et al., 2004a). Since all the faults got fractured finally at the disjointed zone, a circle covering the disjointed region is defined as the resampling region, as in the left-hand side of Figure 17. It could be known from the right-hand side of Figure 17 that the IRR from loaded samples is related with load stress, and the evolution stage could be classified into five stages (I~V) relating with initial compacting, elastic deforming, stress blocking, stress deblocking and rock fracturing respectively. From stage-II to stage-IV, the evolution of AIR*T* has the features of rising to dropping, and to rising again.

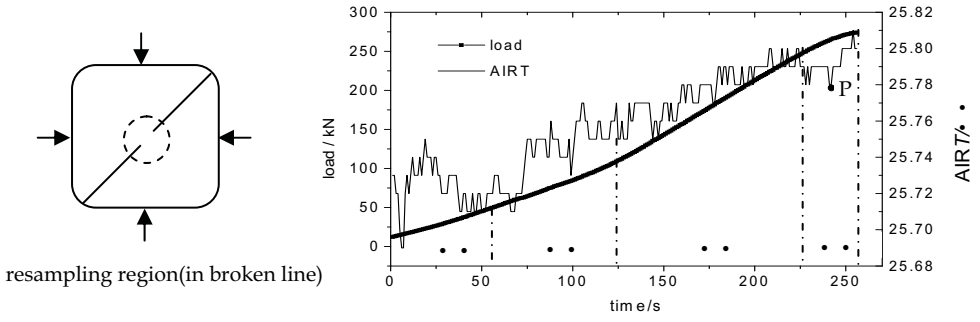

a) collinearly disjointed faults

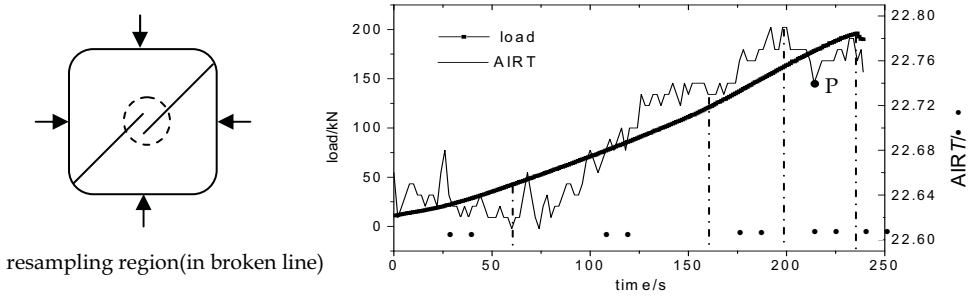

b) en echelon disjointed

Fig. 17. The typical AIR*T* evolution of two kinds of disjointed faults bi-axially loaded

3) The influence of rock characteristics

It was discovered in our experiments that for the most of rock samples in condition of uni-axial loading, its AIR*T* approximately rose with loading. But there were a few abnormal samples made from limestone had shown AIR*T* features of dropping with loading, as in Figure 18. The cause lies in that limestone has much more pores than the other rocks. Usually, there are many gases, such as CH_4, CO_2, CO and O_2 etc., enclosed inside the pores of rock body (Wang, 2003). With the decrement of pore volume due to the loading compaction and with the increment of fractures produced inside the limestone sample, the pore gases will get escaping. The escaping behavior of pore gas needs to absorb thermal energy from the rock sample. If the heat from compression and friction is lower than that absorbed by pore gases, the surface AIR*T* is to drop with loading. If look carefully at the load-displacement curves in Figure 14, it could be founded that the curve of limestone concaved downward the most at the compaction stage as compared to that of the other four kinds of rock, which means that there are more pores inside limestone than the others.

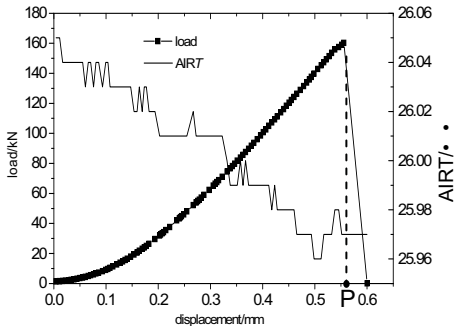

Fig. 18. AIR*T* of uni-axially loaded limestone sample

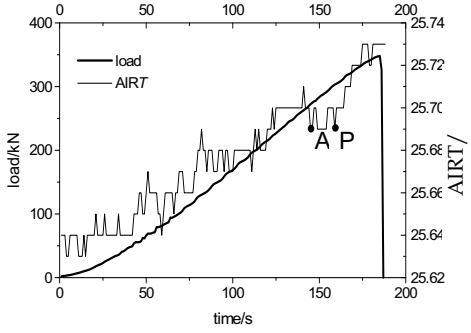

Fig. 19. AIR*T* short-dropping precursor for uni-axially loaded gabbro sample

2.3.3 The classification of precursors

Analysis to the evolution of AIR*T* curves discovered that a large amount of rock samples in condition of uni-axial loading, compressively-sheared loading and bi-axial loading had presented obvious precursors for rock fracturing. As referring to the general process of AIR*T* evolution, the AIR*T* anomaly precursors for rock fracturing and hazard could be classified as short-dropping, rapid-rising and dropping-to-rising respectively.

1) Short-dropping precursor

The AIR*T* curve rises with loading but has a short dropping at loading stage-IV; later, the AIR*T* curve will rise again. The bi-axially load on collinearly and non-collinearly disjointed faults had shown short-dropping precursors as in Figure 17, and the point P was suggested to be the precursor point of rock fracturing and rock hazard. Figure 19 shows another typical case of gabbro sample uni-axially loaded. Here, point A is the turning point of AIR*T* from rising to short dropping, and point P is another turning point from short dropping to rising again, which is suggested to be the precursor point of rock fracturing and rock hazard.

2) Rapid-rising precursor

The AIR*T* curve rises slowly with loading but turns to rise rapidly before rock fracturing, and the turning point is exactly the precursor point. Figure 15 and Figure 16a have this kind of precursor. Figure 20 shows another typical case of marble sample uni-axially loaded. Here, point P is the turning point of AIR*T* from rising slowly to rising fast, which is suggested to be the precursor point of rock fracturing and rock hazard.

3) Dropping-to-rising precursor

The AIR*T* curve drops slowly with loading but turns to rise just before rock fracturing, and the turning point is exactly the precursor point. Figure 16b has this kind of precursor. Figure 21 shows another typical case of marble sample uni-axially loaded. Here, point P is the turning point of AIR*T* from dropping slowly to rising fast, which is suggested to be the precursor point of rock fracturing and rock hazard.

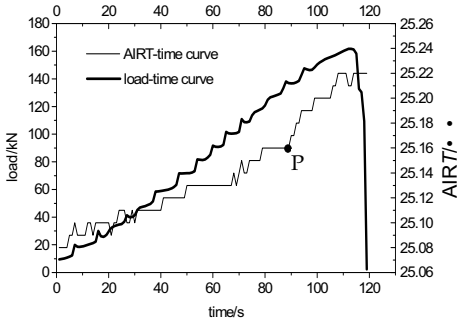

Fig. 20. AIR*T* fast rising precursor for uni-axially loaded marble sample

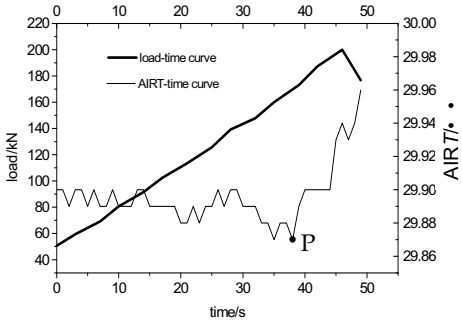

Fig. 21. AIR*T* dropping-to-rising precursor for compressively sheared loaded marble sample

2.3.4 The temporal features of precursors

The occurrence moments of the precursors of AIR*T* of totally 52 tested rock samples are listed in Table 1(Wu et al, 2006b). Although the loading conditions and the rock samples are different, the precursor occurrence moment, were very similar as $0.77\sim0.94\sigma_c(\sigma_p)$. Here, σ_c is the uni-axial compressive strength, and σ_p is the peak stress. The precursor occurrence moment of uni-axially loaded or compressive sheared rock sample is $0.79\sigma_c$ and $0.82\sigma_c$ respectively. It is worthy to mention that the precursor occurrence moment of bi-axially loaded collinearly disjointed faults and echelon faults are much different. That for collinearly disjointed faults was close to the peak stress, $0.87\sigma_p$, while that for echelon faults was far away from peak stress, $0.77\sigma_p$. It provides an important evidence for the complexity of study on tectonic EQ prediction on shock time, based on satellite infrared remote sensing and referring to the seismogenic mechanism.

Loading condition		Sum of tested samples, *St*	Sum of samples with precursors, *Sp*	The ratio: (*Sp*/*St*)• • 100%	Average of precursor occurrence moment
uni-axial loading		22	9	41%	$0.79\sigma_c$
compressively-sheared loading	70• •	7	1	14%	$0.94\sigma_p$
	60• •	8	6	74% 58%	$0.82\sigma_p$
	45• •	11	8	73%	$0.77\sigma_p$
Bi-axial loading for collinearly disjointed faults		2	2	100%	$0.87\sigma_p$
Bi-axial loading for en echelon faults		2	2	100%	$0.77\sigma_p$

Table 1. Statistic for precursor occurrence in different loading conditions

2.4 Large IRR at Fracturing Centre

As the recording rate of the infrared imager applied was 60f/s, the transient IRR

temperature at the fracturing center could be snapped. In condition of uni-axial loading, the fracturing center of a brittle rock is usually at the "X"-shaped fracturing center. It is discovered that the transient IRR temperature at the fracturing center is much higher than that on rock surface, as in Figure 22, and it is positively related with rock strength and rock deformation. For some compressively sheared hard rock samples made from gabbro and gneiss, the transient IRR temperature at the fracturing center is higher than 155°C, which is the upper limitation of the 2nd temperature range (72~155°C) of the imager applied.

In condition of high angle, 60° and 70°, compressively sheared loading, the fracturing center is at the center of the fractured shearing zone. Since the ruptured upper block of rock sample was pushed apart from the steel platen immediately after the abrupt rupturing, usually be 1~2 s after the rupturing, the inside shearing zone got exposed to the imager immediately and the transient IRR temperature filed was snapped. It was discovered that the IRR temperature on the inside shearing zone is not only much higher than that of outside rock surface, but also inhomogeneous distributed, neither even nor centripetal, as in Figure 23. It means that much more mechanical energy had been converted into frictional thermal and IRR energy due to the intensive energy accumulation, the sufficient local deformation and the abrupt frictional sliding at the center of the shearing zone. In other words, the large IRR temperature at the inside shearing center had reflected the comprehensive effect of local concentrated energy conversion and frictional thermal.

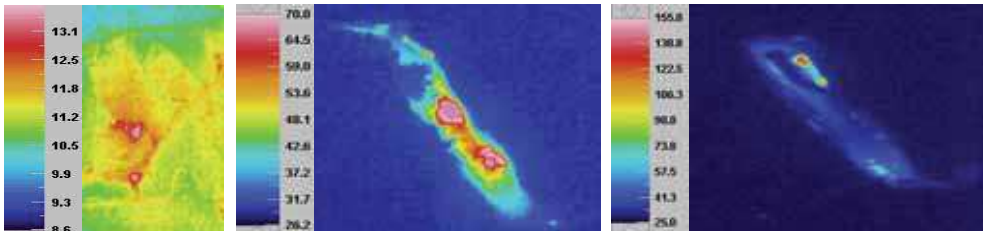

a) uni-axially loaded granite b) compressively sheared gabbro-1 c) compressively sheared gabbro-2

Fig. 22 The transient IRR thermograme of fracturing rock samples

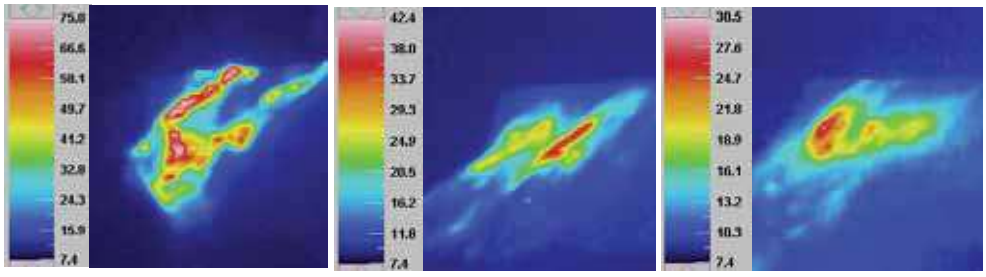

(a) marble-1 (b) marble-2 (c) granite

Fig. 23. The inside IRR isothermal filed on the fracturing zone of compressively sheared rock samples

Hence, it could be deduced that in condition of great tectonic stress, large deformation

and/or abrupt frictional sliding, large temperature as high as hundreds or thousands of degree Celsius is possible inside crust rocks. The high temperature could cause partial melt of crust rock, which provides a scientific explanation for the existence of pseudotachylyte in some lager faults (Nicolas et al., 1977; Sibson et al, 1980) and for the failure-generated EQ lights (Martelli et al., 1989). Besides, we can deduce that the continuous shearing deformation or the abrupt fracturing of highly loaded rock/coal body in a coal mine is possible to cause local sheared heating of temperature hundreds of degree Celsius, which might be a potential ignition of local methane (the minimum ignition temperature is 595^{o}C).

3. Remote Sensing Rock Mechanics Model (RSRM-model)

3.1 Thermo-Mechanical Coupling Effect

3.1.1 Thermo-mechanical coupling in a loaded solid

The heat production inside a loaded solid is called as thermo-mechanical coupling effect. According to the material features and the different deformation stages of a loaded solid, the thermo-mechanical coupling is classified as thermo-elastic, thermo-plastic and thermo-viscous respectively for elastic deformation, plastic deformation and viscous deformation. Generally the rock is a hard brittle solid, its plastic and viscous deformation could be ignored, and the thermo-elastic effect and the frictional thermal are the two chief mechanisms of surface IRR from loaded rock. Kelvin coined the thermo-elastic theory in 1853 that the changed physical temperature of a loaded component is correlated to its changed stress as follows:

$$\Delta T / T = -K_0 \Delta\sigma \tag{1}$$

Here: T is the absolute temperature of a loaded component (K); ΔT is the changed temperature (K); K_0 is the thermo-elastic factor (MPa^{-1}); and $\Delta\sigma$ is the changed sum of three principal stresses ($\sum\sigma_i, i = 1,2,3$, MPa).

As for an isotropic linear elastic solid loaded bi-axially with a free surface, the surface physical temperature variation is tightly correlated with the sum of two principal stresses ($\sum\sigma_i, i = 1,2$):

$$\Delta T = -\alpha / \rho C_p \cdot [T \cdot \Delta(\sigma_1 + \sigma_2)] \tag{2}$$

Here: T is the surface absolute temperature of a loaded solid (K); ΔT is the changed temperature (K); α is the factor of linear expansion (K^{-1}); ρ is the solid density (Kg $\cdot$ m^{-3}); Cp is thermal capacity of solid at normal atmosphere (J $\cdot$ Kg^{-1} $\cdot$ K^{-1}); σ_1 and σ_2 are the two principal stresses (MPa). The thermo-elastic factor K is defined as $K = -\alpha / \rho C_p$.

For the mechanism of stress measurement with TSA and SPATE, the relationship between the stress increment and the IRR signal based on equation (2) is as follows (Mounatin and Webber, 1978):